



## Research Paper

## Thermoelasticity and stability of natural epidote at high pressure and high temperature: Implications for water transport during cold slab subduction

Bo Li<sup>a,b</sup>, Jingui Xu<sup>a,c</sup>, Dongzhou Zhang<sup>c</sup>, Zhilin Ye<sup>a,b</sup>, Shijie Huang<sup>a,b</sup>, Dawei Fan<sup>a,\*</sup>, Wenge Zhou<sup>a</sup>, Hongsen Xie<sup>a</sup><sup>a</sup> Key Laboratory of High Temperature and High Pressure Study of the Earth's Interior, Institute of Geochemistry, Chinese Academy of Sciences, Guiyang 550081, China<sup>b</sup> University of Chinese Academy of Sciences, Beijing 100049, China<sup>c</sup> Hawaii Institute of Geophysics and Planetology, School of Ocean and Earth Science and Technology, University of Hawaii at Manoa, Honolulu, HI, 96822, USA

## ARTICLE INFO

## Keywords:

Epidote  
Hydrous mineral  
Subduction zone  
High-pressure and high-temperature  
Single-crystal X-ray diffraction

## ABSTRACT

Epidote is a typical hydrous mineral in subduction zones. Here, we report a synchrotron-based single-crystal X-ray diffraction (XRD) study of natural epidote  $[\text{Ca}_{1.97}\text{Al}_{2.15}\text{Fe}_{0.84}(\text{SiO}_4)(\text{Si}_2\text{O}_7)\text{O}(\text{OH})]$  under simultaneously high pressure-temperature (high  $P$ - $T$ ) conditions to  $\sim 17.7$  GPa and 700 K. No phase transition occurs over this  $P$ - $T$  range. Using the third-order Birch-Murnaghan equation of state (EoS), we fitted the pressure-volume-temperature ( $P$ - $V$ - $T$ ) data and obtained the zero-pressure bulk modulus  $K_0 = 138(2)$  GPa, its pressure derivative  $K'_0 = 3.0(3)$ , the temperature derivative of the bulk modulus  $(\partial K/\partial T)_P = -0.004(1)$  GPa/K, and the thermal expansion coefficient at 300 K ( $\alpha_0 = 3.8(5) \times 10^{-5}$  K<sup>-1</sup>), as the zero-pressure unit-cell volume  $V_0$  was fixed at 465.2(2) Å<sup>3</sup> (obtained by a single-crystal XRD experiment at ambient conditions). This study reveals that the bulk moduli of epidote show nonlinear compositional dependence. By discussing the stabilization of epidote and comparing its density with those of other hydrous minerals, we find that epidote, as a significant water transporter in subduction zones, may maintain a metastable state to  $\sim 14$  GPa along the coldest subducting slab geotherm and promote slab subduction into the upper mantle while favoring slab stagnation above the 410 km discontinuity. Furthermore, the water released from epidote near 410 km may potentially affect the properties of the 410 km seismic discontinuity.

## 1. Introduction

Hydrous minerals play a crucial role in carrying and storing H<sub>2</sub>O in the deep Earth (e.g., Pawley et al., 1996; Schmidt and Poli, 1998; Peacock and Hyndman, 1999; Hacker et al., 2003; Faccenda, 2014; Zheng et al., 2016, 2019; Mookherjee et al., 2019; Xu et al., 2019a; Zhang et al., 2019). They are also involved in the progressive dehydration of a subducting slab. This process is considered responsible for intermediate-depth earthquakes (Kirby et al., 1996; Peacock, 2001) and can trigger hydration-driven partial melting reactions in the mantle wedge above the slab, further leading to explosive volcanism (Peacock, 1990; Schmidt and Poli, 1998; Forneris and Holloway, 2003). The physical and chemical properties of hydrous minerals can restrict their stability and the pressure-temperature ( $P$ - $T$ ) conditions of the related dehydration reactions in which they are potentially involved (Pawley et al., 1998; Hacker et al., 2003; Alvaro et al., 2012; Liu et al., 2019b).

Consequently, an exhaustive study of the physical and chemical properties of hydrous minerals, in particular, their thermoelastic properties under high  $P$ - $T$  conditions, is an essential prerequisite for an accurate understanding of the geodynamic processes in the Earth's mantle and subduction zones (e.g., Fan et al., 2011; Alvaro et al., 2012; Kakizawa et al., 2018; O'Bannon et al., 2018; Liu et al., 2019a; Satta et al., 2019; Bindi et al., 2020).

Epidote, a geologically significant hydrous Ca–Al-silicate, mainly occurs in many metabasites, metapelites and metacherts that are typical in subduction zones (Liou, 1973, 1993; Bird and Spieler, 2004; Enami et al., 2004; Chen et al., 2019). As an important carrier of water in subduction zones (Schmidt and Poli, 1998; Spandler et al., 2003; Enami et al., 2004; Frei et al., 2004), epidote contains  $\sim 2$  wt.% H<sub>2</sub>O and typically up to 5–20 wt.% in subducting mid-ocean ridge basalts (MORB) (Schmidt and Poli, 1998). It belongs to the monoclinic epidote-group minerals with mixed SiO<sub>4</sub> tetrahedra and Si<sub>2</sub>O<sub>7</sub> groups and has a

\* Corresponding author.

E-mail address: [fandawei@vip.gyig.ac.cn](mailto:fandawei@vip.gyig.ac.cn) (D. Fan).

Peer-review under responsibility of China University of Geosciences (Beijing).

<https://doi.org/10.1016/j.gsf.2020.05.022>

Received 7 January 2020; Received in revised form 22 March 2020; Accepted 20 May 2020

Available online 5 August 2020

1674-9871/© 2020 China University of Geosciences (Beijing) and Peking University. Production and hosting by Elsevier B.V. This is an open access article under the

CC BY-NC-ND license (<http://creativecommons.org/licenses/by-nc-nd/4.0/>).

topology consistent with space group  $P2_1/m$  (Franz and Liebscher, 2004). The general chemical formula of epidote can be expressed as  $A1A2M1M2M3(SiO_4)(Si_2O_7)O(OH)$ , where A1 and A2 are sites with coordination numbers larger than 6 and are usually filled with  $Ca^{2+}$ , and M1, M2, and M3 are octahedral sites mainly occupied by  $Al^{3+}$  and  $Fe^{3+}$ . The  $Fe^{3+}$  content of epidote is expressed as  $X_{Ep} = Fe^{3+}/(Fe^{3+} + Al^{3+} - 2)$ , and commonly,  $X_{Ep}$  is in the range of 0.5–1.0 (Franz and Liebscher, 2004). The crystal structure of epidote (Fig. 1) is built up by two types of repeating octahedrons that run parallel to the  $b$ -axis and consists of three non-equivalent octahedrons M1, M2, and M3. One type of octahedral chain is made up only of edge-sharing M2 octahedra, while M1 and M3 octahedra attach on alternate sides along the chain extension to form another chain. These two octahedral chains are cross-linked in [100] and [001] by isolated  $SiO_4$  and  $Si_2O_7$  groups with two nonequivalent large A1 and A2 positions in between (Franz and Liebscher, 2004).

Several authors have studied the equation of state (EoS) of epidote by means of X-ray diffraction (XRD) on samples with different Fe contents and obtained diverse values for the bulk modulus  $K_0$  and its pressure derivative  $K'_0$ . Holland et al. (1996) conducted a powder XRD study of a natural epidote sample with composition  $X_{Ep} = 1.0$  up to 5.21 GPa and

obtained a value of  $K_0 = 162(4)$  GPa with  $K'_0$  fixed at 4. Subsequently,  $K_0 = 207(15)$  GPa was obtained by Qin et al. (2003) with  $K'_0$  fixed at 4 on a natural epidote sample ( $X_{Ep} = 0.6$ ) up to 20 GPa. For a natural epidote sample with  $X_{Ep} = 0.74$ , Gatta et al. (2011) obtained  $K_0 = 111(3)$  GPa and  $K'_0 = 7.6(7)$  up to 10 GPa (at 300 K) and volume thermal expansion coefficient  $\alpha_T = 5.1(2) \times 10^{-5} - 5.1(6) \times 10^{-4} T^{-1/2}$  up to 1200 K (at 0.0001 GPa). In addition, Fan et al. (2014) obtained  $K_0 = 116(7)$  GPa and its pressure derivative  $K'_0 = 7.8(8)$  on a natural epidote sample with  $X_{Ep} = 0.5$  up to 9.16 GPa. Recently,  $K_0 = 115(3)$  GPa and  $K'_0 = 3.7(2)$  was gained by Qin et al. (2016) on a natural epidote sample ( $X_{Ep} = 0.79$ ) up to 30 GPa. In this light, the thermoelastic properties of epidote under simultaneously high  $P$ - $T$  conditions have not yet been evaluated, which hinders our understanding of the thermoelasticity and stability of epidote in the deep Earth, especially within subduction zones.

In this study, we report the pressure-volume-temperature ( $P$ - $V$ - $T$ ) relations of natural epidote  $[Ca_{1.97}Al_{2.15}Fe_{0.84}(SiO_4)(Si_2O_7)O(OH)]$  under simultaneously high  $P$ - $T$  conditions up to  $\sim 17.7$  GPa and 700 K using an *in situ* synchrotron-based single-crystal XRD method in an externally heated diamond anvil cell (EHDAC). The chemical composition of the sample reflects the typical epidote composition in ultrahigh-

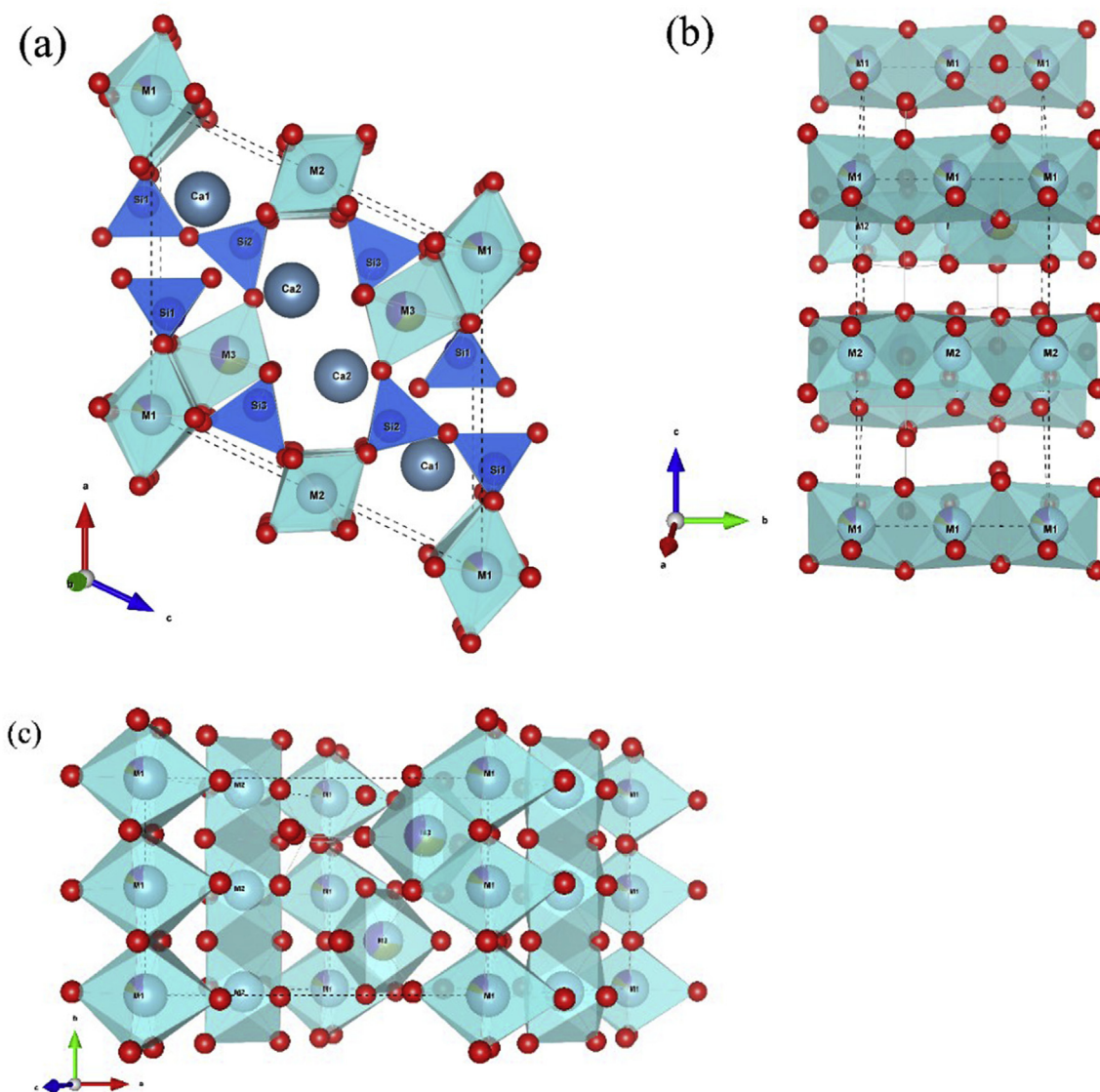


Fig. 1. Crystal structure of epidote viewed along the  $b$ -axis (a),  $a$ -axis (b),  $c$ -axis (c); the red balls indicate oxygen, and the cyan balls indicate calcium. In this structure,  $Si^{4+}$  occupies tetrahedral sites. M1, M2 and M3 represent three types of octahedral sites; M2 is occupied by  $Al^{3+}$ , while M1 and M3 can be occupied by  $Al^{3+}$  and  $Fe^{3+}$  (color online).

pressure (UHP) metamorphic belts (Ferrando et al., 2005; Cao and Song, 2009; Guo et al., 2013). By fitting the present  $P$ - $V$ - $T$  data to the high-temperature Birch-Murnaghan EoS, we obtain the thermoelastic parameters of epidote. In addition, our results are compared with those of previous studies of epidote with different Fe contents. Finally, we discuss the stability of epidote and the potential implications for water transport during cold slab subduction.

## 2. Sample and experiment

A natural, dark green epidote sample used in this study was collected from Yunnan Province in China. The chemical composition of the epidote was estimated as  $[\text{Ca}_{1.97}\text{Al}_{2.15}\text{Fe}_{0.84}(\text{SiO}_4)(\text{Si}_2\text{O}_7)\text{O}(\text{OH})]$  based on the results of electron microprobe analysis (EMPA) using a JXA-8230 electron microprobe. The analytic acceleration voltage was 15 kV, the beam current was 20 nA, and the beam size was 5  $\mu\text{m}$  in diameter. A small chip of a single epidote crystal with a thickness of less than 10  $\mu\text{m}$  was extracted from a larger EMPA sample for this study.

High  $P$ - $T$  XRD experiments were carried out using an EHDAC (Kantor et al., 2012), which was equipped with a pair of 500- $\mu\text{m}$  culet-size diamond anvils mounted on wolfram carbide (WC) seats. A rhenium foil, pre-indented to a thickness of  $\sim 50$   $\mu\text{m}$ , was used as a gasket, and a hole with a diameter of 300  $\mu\text{m}$  was drilled to serve as the sample chamber. The epidote sample was loaded into the sample chamber with Au powder serving as the pressure calibrant (Fei et al., 2007). At each  $P$ - $T$  point, the Au diffraction patterns were obtained before and after sample data collection, and the pressure uncertainties did not vary by more than  $\pm 0.1$  GPa. The neon pressure medium was loaded into the sample chamber using the gas-loading system at the GeoSoilEnviroConsortium for Advanced Radiation Sources (GSECARS) of the Advanced Photon Source (APS), Argonne National Laboratory (ANL) (Rivers et al., 2008). After neon gas loading, the gasket hole shrank to approximately 200  $\mu\text{m}$  in diameter, and the initial pressure was approximately 0.5 GPa. Heating was carried out by a resistance-heating system, and the temperature was measured with a Pt<sub>90</sub>Rh<sub>10</sub>–Pt<sub>100</sub> thermocouple attached to one of the diamond anvils approximately 500  $\mu\text{m}$  from the diamond culet (Xu et al., 2018, 2019b; Fan et al., 2019a, b), and the uncertainty involved in temperature measurement was less than 1 K (Sinogeikin et al., 2006; Fan et al., 2010; J. Yang et al., 2014b; Mao et al., 2015). To minimize the temperature instability for each heating run, we stabilized the sample chamber at a given temperature for at least 600 s. Temperatures of the sample chamber were actively stabilized within  $\pm 1$  K using the temperature-power feedback program with a remotely controlled DC power supply during the experiments (Zhang et al., 2017).

The high  $P$ - $T$  single-crystal XRD measurements were conducted at beamline 13-BM-C of the APS. The incident X-ray beam had a wavelength of 0.4340  $\text{\AA}$  and a focal spot size of 15  $\mu\text{m} \times 20$   $\mu\text{m}$  full widths at half maximum (FWHM). The MAR165 charge-coupled device (CCD) detector (Zhang et al., 2017) was placed approximately 156 mm from the sample to acquire the diffraction images, and ambient LaB<sub>6</sub> powder was used to calibrate the distance and tilt of the detector. Wide and stepped  $\phi$ -rotation exposures were collected for the single-crystal sample at each loading run, with an exposure time of 2 s/deg. The  $\phi$ -rotation axis was horizontal and perpendicular to the incident X-ray direction.

The XRD images at each  $P$ - $T$  point were analyzed using the GSE ADA/RVS software package (Dera et al., 2013). Then, the unit-cell parameters of epidote were refined by the least-squares fitting technique using the *UnitCell* software (Holland and Redfern, 1997). Each diffraction pattern had at least 30 good single-crystal diffraction spots. Except for the single-crystal diffraction spots of the diamond, all the other single-crystal diffraction spots could be successfully indexed using the monoclinic symmetry of epidote. The obtained characteristic diffraction peaks of epidote were (-211), (020), (120), (-311), (-221), (-321), (-502), (-231), (-206), (115), and (040). Only the peaks appearing at all  $P$ - $T$  steps were used to refine the unit-cell parameters to maintain consistency. The unit-cell parameters obtained in this study (Table 1) had high quality

consistent with that of recent studies (Gatta et al., 2011; Qin et al., 2016).

## 3. Results and discussion

Single-crystal XRD patterns of epidote are shown in Fig. 2. No phase transition was observed up to the maximum  $P$ - $T$  conditions in this study ( $\sim 17.7$  GPa and 700 K). The refined unit-cell parameters of epidote at various  $P$ - $T$  conditions are shown in Table 1. To derive the thermoelastic parameters from the measured  $P$ - $V$ - $T$  data, we first fitted the compressional  $P$ - $V$  data at the 300 K isotherm to the Birch-Murnaghan EoS and then applied the high-temperature Birch-Murnaghan EoS fitting approach.

**Table 1**  
Unit-cell parameters of epidote at different pressures and temperatures.

$P$ (GPa)	$T$ (K)	$V$ ( $\text{\AA}^3$ )	$a$ ( $\text{\AA}$ )	$b$ ( $\text{\AA}$ )	$c$ ( $\text{\AA}$ )	$\beta$ ( $^\circ$ )
0.0001	300	456.2(2)	8.875(3)	5.610(1)	10.130(4)	115.26(4)
0.5(1)	300	454.8(2)	8.866(3)	5.603(1)	10.123(4)	115.27(4)
2.3(1)	300	448.5(2)	8.823(3)	5.578(1)	10.070(4)	115.20(4)
4.5(1)	300	442.1(2)	8.780(3)	5.552(1)	10.023(4)	115.20(4)
5.8(1)	300	438.3(2)	8.751(3)	5.537(1)	9.998(3)	115.22(4)
6.3(1)	300	436.8(2)	8.740(3)	5.533(1)	9.982(3)	115.17(4)
8.4(1)	300	431.6(2)	8.702(3)	5.513(1)	9.936(3)	115.11(4)
11.1(1)	300	424.6(2)	8.643(2)	5.490(1)	9.870(3)	114.95(4)
12.2(1)	300	421.6(2)	8.614(2)	5.480(1)	9.852(3)	114.97(4)
15.0(1)	300	415.0(2)	8.564(2)	5.458(1)	9.776(3)	114.73(4)
4.4(1)	500	445.8(2)	8.804(3)	5.567(1)	10.054(4)	115.21(4)
5.8(1)	500	441.6(2)	8.774(3)	5.550(1)	10.021(3)	115.20(4)
6.9(1)	500	438.4(2)	8.749(3)	5.539(1)	9.995(3)	115.17(4)
7.8(1)	500	435.6(2)	8.730(3)	5.528(1)	9.969(3)	115.12(4)
8.3(1)	500	434.7(2)	8.723(3)	5.525(1)	9.961(3)	115.11(4)
9.5(1)	500	431.2(2)	8.695(2)	5.513(1)	9.932(3)	115.09(4)
10.7(1)	500	428.6(2)	8.677(2)	5.502(1)	9.907(3)	115.03(4)
12.4(1)	500	424.0(2)	8.638(2)	5.488(1)	9.866(3)	114.97(4)
14.3(1)	500	420.1(2)	8.606(2)	5.473(1)	9.837(3)	114.95(4)
16.3(1)	500	414.5(2)	8.558(2)	5.456(1)	9.776(3)	114.76(4)
7.0(1)	700	440.7(2)	8.765(3)	5.549(1)	10.007(3)	115.12(4)
9.1(1)	700	435.0(2)	8.723(3)	5.527(1)	9.965(3)	115.13(4)
11.5(1)	700	429.0(2)	8.675(2)	5.508(1)	9.910(3)	115.05(4)
13.8(1)	700	423.4(2)	8.634(2)	5.486(1)	9.861(3)	114.96(4)
17.7(1)	700	414.2(2)	8.557(2)	5.453(1)	9.777(3)	114.79(4)

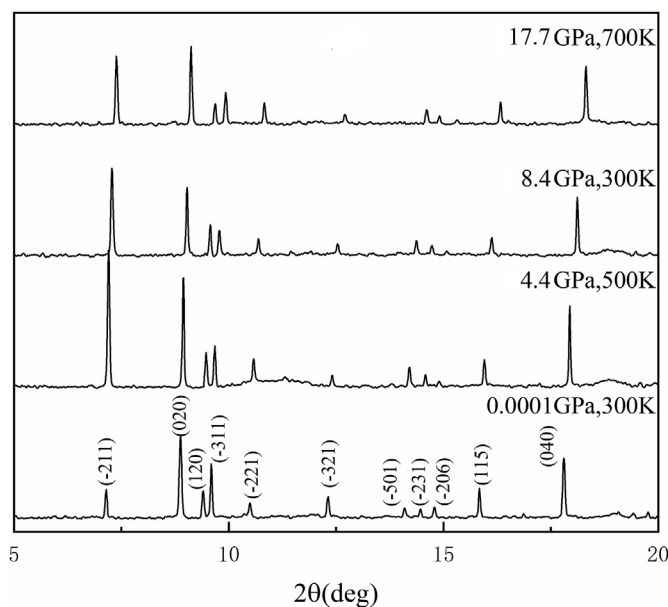


**Fig. 2.** Representative X-ray diffraction patterns (single-crystal XRD) of epidote under high  $P$ - $T$  conditions.



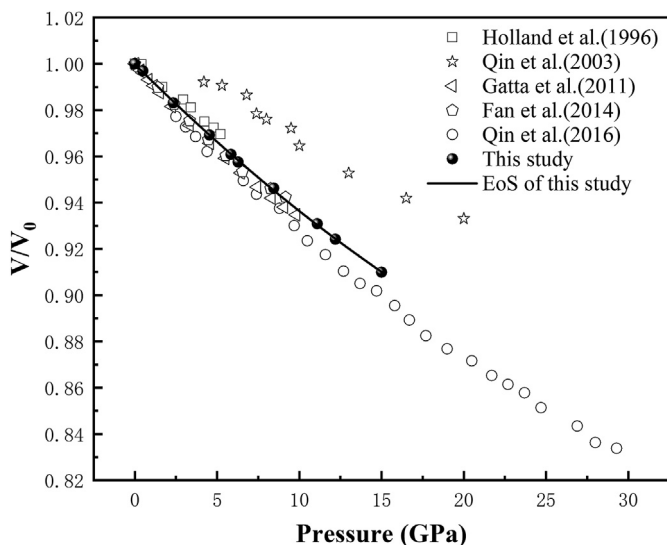


Fig. 3. Normalized unit-cell volume of epidote as a function of pressure at 300 K. The black solid line represents the BM3 EoS fitting based on all data from this study. The error bars are smaller than the symbols for this study.

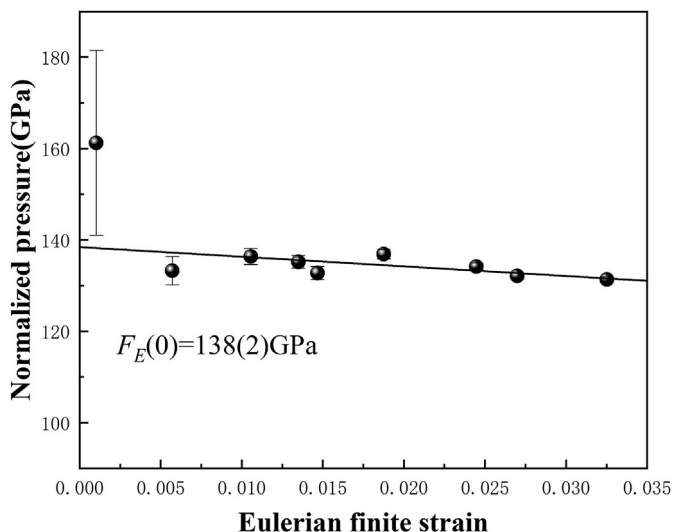


Fig. 4. Eulerian strain-normalized pressure ( $F_E-f_E$ ) plot of the unit-cell volume of epidote.

### 3.1. Pressure-volume data at 300 K

**Birch-Murnaghan equation of state.** The  $P$ - $V$  relations were determined by fitting the present 300 K data to a third-order Birch-Murnaghan

EoS, which is embodied as follows:

$$P = (3/2)K_0 \left[ \left( \frac{V_0}{V} \right)^{2/3} - \left( \frac{V_0}{V} \right)^{5/3} \right] \times \left[ 1 + \left( \frac{3}{4} \right) (K'_0 - 4) \left[ \left( \frac{V_0}{V} \right)^{2/3} - 1 \right] \right] \quad (1)$$

where  $V_0$ ,  $K_0$ , and  $K'_0$  are the unit-cell volume, isothermal bulk modulus, and its pressure derivative under ambient conditions, respectively. Since we obtained the unit-cell parameters of epidote under ambient conditions through single-crystal XRD (Table 1),  $V_0 = 456.2(2) \text{ \AA}^3$  was always fixed in the fitting of the EoS. Analyses of Eq. (1) by the EoSFit 7c program (Angel et al., 2014) with all parameters free yielded  $K_0 = 138(2)$  GPa and  $K'_0 = 3.0(3)$  for epidote. With  $K'_0$  fixed at 4, the fitting results yielded  $K_0 = 133.1(7)$  GPa. Fig. 3 shows the EoS curve derived from the fitting of the  $P$ - $V$  data and compares it with the results reported in previous studies (Holland et al., 1996; Qin et al., 2003, 2016; Gatta et al., 2011; Fan et al., 2014). The volume Eulerian finite strain ( $f_E = [(V_0/V)^{2/3} - 1]$ ) vs. “normalized pressure” ( $F_E = P/[3f_E(2f_E + 1)^{5/2}]$ ) plot (Angel, 2000) was also used to analyze the  $P$ - $V$  data, and a weighted linear fitting yielded an intercept value of 138(2) GPa, which is in good agreement with the results indicated by the third-order Birch-Murnaghan EoS within the uncertainty (Fig. 4). Furthermore, the normalized pressure as a function of the Eulerian strain at 300 K has a negative slope (Fig. 4), which is consistent with a value of  $K'_0$  slightly less than 4 (Angel, 2000). Therefore, the third-order Birch-Murnaghan EoS is a reasonable choice of the EoS for fitting of the  $P$ - $V$  data (Angel, 2000).

**Vinet equation of state.** We also analyzed the  $P$ - $V$  data using the Vinet EoS (Vinet et al., 1986), which is derived from a “universal equation” for solids and is represented as follows:

$$P(V) = 3K_0y^{-2}(1 - y)\exp[\eta_0(1 - y)] \quad (2)$$

where  $y = x^{1/3}$ ,  $x = V/V_0$  and  $\eta_0 = (3/2)(K'_0 - 1)$ . Analyses of Eq. (2) yielded  $K_0 = 138(2)$  GPa, and  $K'_0 = 3.0(3)$  for epidote, which are excellently consistent with those derived by fitting to the Birch-Murnaghan EoS.

From Table 2, we can find that the  $K_0 = 207(15)$  GPa of epidote reported by Qin et al. (2003) is larger than other values. The leading cause may be the pressure-transmitting medium (16:3:1 methanol-ethanol-water mixture) used in their study. The 16:3:1 methanol-ethanol-water mixture as a pressure-transmitting medium can maintain an excellent hydrostatic pressure ambience only under 10 GPa (Angel et al., 2007), while the maximum pressure reached 20 GPa in their study. However, our result of  $K_0 = 138(2)$  GPa is distinctly higher than 111(3) GPa reported by Gatta et al. (2011), 116(7) GPa by Fan et al. (2014), and 115(2) GPa by Qin et al. (2016) and less than 162(4) GPa obtained by Holland et al. (1996). The possible reasons for this difference may be multiple and complicated (Supplementary Material) (Allen, 1989; Comodi and Zanazzi, 1997; Fehr and Heuss-Aßbichler, 1997; Zhang, 1999; Franz and Liebscher, 2004; Gottschalk, 2004; Gatta et al.,

Table 2  
Summary of thermoelastic studies of epidote.

$X_{Ep}$	$K_0$ (GPa)	$K'_0$	$V_0$ ( $\text{\AA}^3$ )	$\alpha_0$ ( $\text{K}^{-1}$ )	$(\partial K/\partial T)_P$	Methods	$P_{\max}$ (GPa), $T_{\max}$ (K)	Pressure medium	Reference
1.0	162(4)	4(fixed)	459.9(3)			XRD(PD) <sup>a</sup>	5.12, 298	ME = 4:1 <sup>c</sup>	Holland et al. (1996)
0.6	207(15)	4(fixed)				XRD(PD)	20, 298	MEW = 16:3:1	Qin et al. (2003)
0.74	111(3)	7.6(7)	458.8(1)			XRD(PD)	10, 298	MEW = 16:3:1	Gatta et al. (2011)
0.74				$2.15 \times 10^{-5}$		XRD(PD)	0.0001, 1200		Gatta et al. (2011)
0.5	116(7)	7.8(8)	463.8(6)			XRD(PD)	9.16, 298	MEW = 16:3:1 <sup>d</sup>	Fan et al. (2014)
0.5	132(4)	4(fixed)				XRD(PD)	9.16, 298	MEW = 16:3:1	Fan et al. (2014)
0.79	115(2)	3.7(2)	461.1(1)			XRD(SC) <sup>b</sup>	29.4, 298	Neon	Qin et al. (2016)
0.79	112.2(4)	4(fixed)	461.1(1)			XRD(SC)	29.4, 298	Neon	Qin et al. (2016)
0.84	138(2)	3.0(3)	456.2(2)			XRD(SC)	15, 300	Neon	This study
0.84	133.1(7)	4(fixed)	456.2(2)	$3.8(5) \times 10^{-5}$	-0.004(1)	XRD(SC)	17.7, 700	Neon	This study

a: Powder X-ray diffraction; b: Single-crystal X-ray diffraction; c: 4:1 methanol-ethanol mixture; d: 16:3:1 methanol-ethanol-water mixture.

2011; Fan et al., 2013a, 2013b, 2014, 2015; Huang and Chen, 2014; Qin et al., 2016; Xu et al., 2017a, 2017b).

### 3.2. Pressure-volume-temperature data and thermoelastic parameters

The *P-V-T* data (Table 1) were used to determine the thermoelastic parameters of epidote up to ~17.7 GPa, and 700 K. Fig. 5 shows the volume data measured at 300, 500, and 700 K. The high-temperature Birch-Murnaghan (HTBM) EoS was applied to our high *P-T* data with the following form:

$$P = (3/2)K_{T0} \left[ \left( \frac{V_{T0}}{V} \right)^{7/3} - \left( \frac{V_{T0}}{V} \right)^{5/3} \right] \times \left[ 1 + \left( \frac{3}{4} \right) (K'_{T0} - 4) \left[ \left( \frac{V_{T0}}{V} \right)^{2/3} - 1 \right] \right] \quad (3)$$

where  $V_{T0}$ ,  $K_{T0}$ , and  $K'_{T0}$  are the unit-cell volume, isothermal bulk modulus, and its pressure derivative under ambient conditions, respectively. The effects of temperature on  $K_{T0}$  and  $V_{T0}$  are expressed as follows:

$$V_{T0} = V_0 \exp \int_{300}^T \alpha_T dT \quad (4)$$

$$K_{T0} = K_0 + (\partial K_0 / \partial T)_p \times (T - 300) \quad (5)$$

where  $(\partial K_0 / \partial T)_p$  and  $\alpha_T = \alpha_0 + \alpha_1 T$  (Fei, 1995) are the temperature derivative of the bulk modulus and the volumetric thermal expansion at ambient pressure, respectively.

Fitting the *P-V-T* data to the HTBM EoS (3) yielded:  $(\partial K / \partial T)_p = -0.004(1)$  GPa/K and  $\alpha_T = 4.4(5) \times 10^{-5} - 2(1) \times 10^{-8} T$ . The  $K_{T0}$  and  $K'_0$  values were fixed at the results derived from the EoS fitted at 300 K [ $K_0 = 138(2)$  GPa, and  $K'_0 = 3.0(3)$ ].

Previous studies on the thermal expansion of epidote are limited. Only Gatta et al. (2011) investigated the thermoelastic behavior of epidote ( $X_{Ep} = 0.74$ ) and obtained thermal expansion up to 1200 K (at 0.0001 GPa) (Table 2). The thermal expansion coefficient at 300 K obtained here for epidote of  $3.8(5) \times 10^{-5} \text{ K}^{-1}$  ( $X_{Ep} = 0.84$ ) is larger than the value of  $2.15 \times 10^{-5} \text{ K}^{-1}$  ( $X_{Ep} = 0.74$ ) obtained by Gatta et al. (2011).

## 4. Geophysical implications

### 4.1. Epidote stabilization in a cold subduction zone

Epidote can stably exist in crustal rocks and hydrothermally altered basalt in a wide *P-T* range that extends to 4 GPa and more than 1000 °C (Liou, 1993; Enami et al., 2004; Poli and Schmidt, 2004) and can survive to depths up to ~200 km under most types of subduction zone *P-T* conditions (Forneris and Holloway, 2003; Hacker et al., 2003). Although, there has been no evidence to data to demonstrate that epidote could occur at depths greater than ~200 km, the temperature at the surface of the slab is generally higher than that in the interior, which is not beneficial to transporting epidote into the deep Earth. However, several high-pressure XRD studies have indicated that epidote could be stable with no phase transitions at least up to ~30 GPa and room temperature (Gatta et al., 2011; Qin et al., 2016). In this study, the high *P-T* single-crystal XRD experiments on epidote also indicate that no phase transition occurred up to ~17.7 GPa and 700 K, implying that at relatively cold conditions in subduction zones, epidote may remain metastable to depths greater than those obtained from experimental petrology (Forneris and Holloway, 2003; Hacker et al., 2003). For example, epidote may be metastable in the old and rapidly subducting slab in northern Tonga, where the coldest part of the subducting slab (~700 K) could be preserved to a considerable depth (~430 km) based on the subduction zone thermal model (Fig. 6) (Bina and Navrotsky, 2000).

### 4.2. Effect on water transport by slab subduction

During the subduction of oceanic slabs, water is transported by hydrous minerals (e.g., Pawley et al., 1996; Schmidt and Poli, 1998; Peacock and Hyndman, 1999; Hacker et al., 2003; Alvaro et al., 2012; Faccenda, 2014; Zheng et al., 2016; Kakizawa et al., 2018; Liu et al., 2019c) and is supposed to be critical to several geologically essential processes, such as island-arc volcanism (Portnyagin et al., 2007), intermediate-depth seismicity (Green and Houston, 1995), and chemical exchange between the subducting slab and mantle (Ewart et al., 1998). As an important hydrous Ca–Al–silicate in subducting MORB, epidote contains ~2 wt.% H<sub>2</sub>O and typically up to 5–20 wt.% (Schmidt and Poli, 1998). Therefore, the behavior of epidote in subduction zones has great significance for understanding the subduction and exhumation

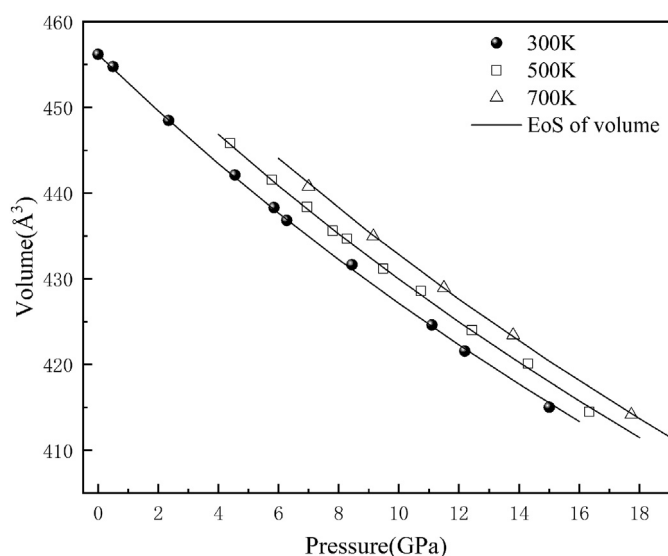


Fig. 5. Unit-cell volume of epidote as a function of pressure and temperature. The solid lines represent the isothermal compression curves from fitting the HTBM EoS at 300 K, 500 K, and 700 K. The error bars of the data points are smaller than the symbols.

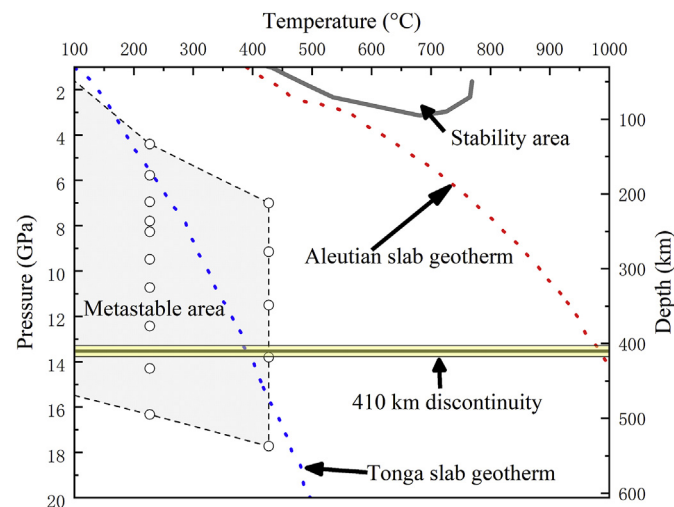
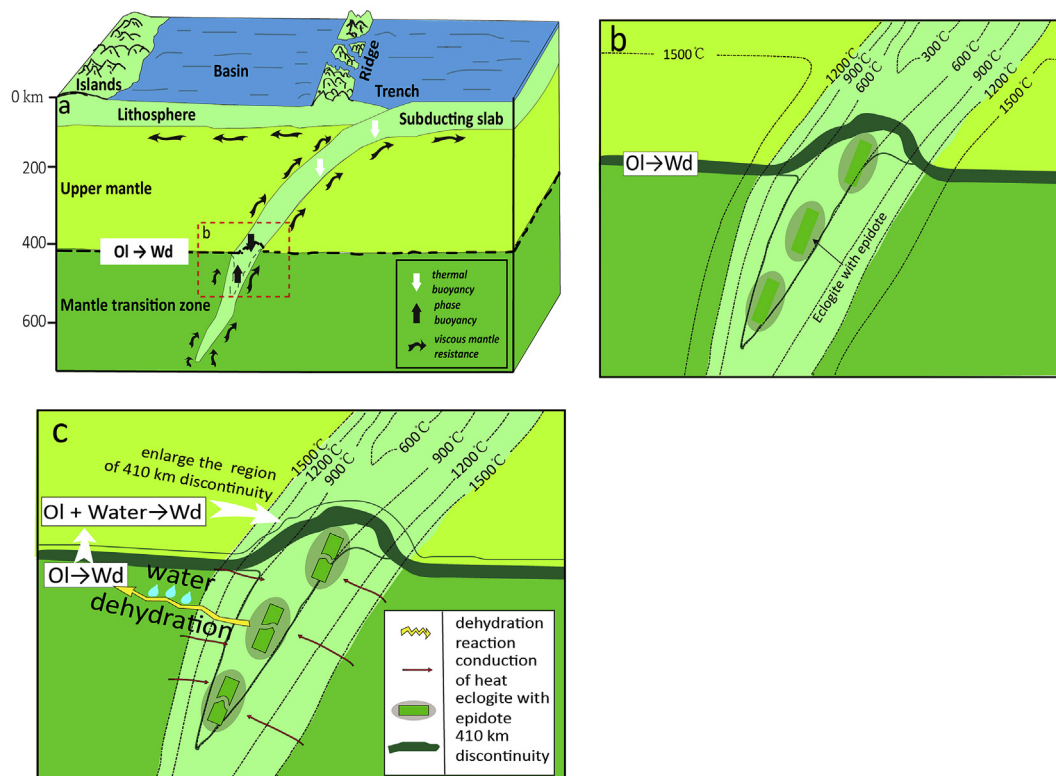


Fig. 6. *P-T* stability estimates for epidote in hydrated MORB compositions. Thick gray lines delineate the stability field of epidote according to Poil and Schmidt (2004). The circles and dashed line show the metastable area of epidote according to our study. The dotted line represents the Tonga slab geotherm (blue) and the Aleutian slab geotherm (red) (Bina and Navrotsky, 2000). The yellow area represents the 410 km discontinuity (color online).



**Fig. 7.** (a) Schematic diagram of the Tonga subduction zone showing the main factors influencing subduction. (b) Epidote is transported to the vicinity of the 410 km discontinuity along the subduction zone. (c) With heat conduction from the surrounding mantle, epidote dehydrates, which affects the  $\alpha$ - $\beta$  phase transition in olivine, thus enlarging the region of the 410 km discontinuity. Ol: olivine, Wd: wadsleyite.

**Table 3**

Thermoelastic properties of epidote and other hydrous minerals used for density calculations.

Mineral	$V_0$ ( $\text{\AA}^3$ )	$K_0$ (GPa)	$K'_0$	$\alpha_0$ ( $10^{-5} \text{ K}^{-1}$ )	$(\partial K/\partial T)_P$	Reference
Epidote	456.2(2)	133.2(6)	4(fixed)	4.3(2)	-0.022(5)	This study
Zoisite	901.0	125.1	4(fixed)	3.4(5)	-0.0128(42)	Grevel et al. (2000)
Lawsonite	674.5	105.9(42)	4.67(169)	3.710(293)	-0.0201(67)	Grevel et al. (2000)
Brucite	40.8(1)	39.6(14)	6.7(7)	5.0(7)	-0.0114(16)	Xia et al. (1998)
Chlorite	701.0	83.4(7)	4(fixed)	2.5(6)	-0.013	Pawley et al. (2002)
Antigorite	366.9(7)	65.2(31)	6.1(fixed)	3.92(5)	-0.0256(41)	Yang et al. (2014a)
Tourmaline	1537.1(11)	96.6(9)	12.5(4)	4.39(27)	-0.009(6)	Xu et al. (2016)

mechanisms of a subduction zone and the water circulation in the upper mantle. Generally, the density difference between the slab and the surrounding mantle is a crucial factor that controls buoyancy (Fig. 7a) (Mierlo et al., 2013; Agrusta et al., 2015; King et al., 2015; Bina, 2016). To better understand the effect of epidote on slab dynamics we calculated the density profiles of epidote and other hydrous minerals (zoisite, lawsonite, tourmaline, brucite, chlorite, and antigorite) (Xia et al., 1998; Grevel et al., 2000; Pawley et al., 2002; C.P. Yang et al. 2014a; Xu et al., 2016), along a geotherm that is typical for cold subduction, such as Tonga (Bina and Navrotsky, 2000; Ganguly et al., 2009). In the calculation, the high-temperature Birch-Murnaghan EoS was used, and the minerals and related thermoelastic parameters are shown in Table 3. The densities of epidote and other hydrous minerals were calculated to a depth of 500 km according to the pressure range of this study.

The modeled density profiles compared with the PREM model (Dziewonski and Anderson, 1981) are presented in Fig. 8. Epidote is the densest of these hydrous minerals, suggesting that it is more conducive to transporting water to deeper locations in the Earth's interior (Fig. 8). At upper mantle depths, epidote group minerals (epidote and zoisite) are denser than PREM. Although the epidote group minerals are the minor minerals in subduction slabs and their effect on the density of the plate

may be limited, they would cause a decrease in buoyancy, thus promoting slab subduction. On the other hand, the epidote group minerals are less dense than PREM at depths greater than 410 km, which is favorable for slab stagnation at the top of the mantle transition zone.

Furthermore, epidote contains far more water than nominally anhydrous minerals, even though its content in the slab is much less than that of nominally anhydrous minerals (Schmidt and Poli, 1998; Zheng et al., 2016). According to the results of our study, epidote may transport a large amount of water to a depth of approximately 410 km (14 GPa) under conditions to those of the coldest subduction zones, e.g., Tonga (Fig. 6). Because the temperature of the surrounding mantle is much higher than that of the subduction slab, the temperature of the subducting slab increases with time, leading to epidote dehydration (Fig. 7b and c). On the other hand, wadsleyite becomes stable at a depth of approximately 410 km, so the water released from epidote dehydration may potentially affect the olivine-wadsleyite phase transition and thus the properties of the 410 km seismic discontinuity (Fig. 7c) (Wood et al., 1996; Bina and Navrotsky, 2000). According to Wood et al. (1996), the effect of water (500 ppm) on the olivine-wadsleyite phase transition is dramatic, and the pressure width of the two-phase region is enlarged from 0.25 GPa in the dry system to 0.8 GPa with 500 ppm water, so that

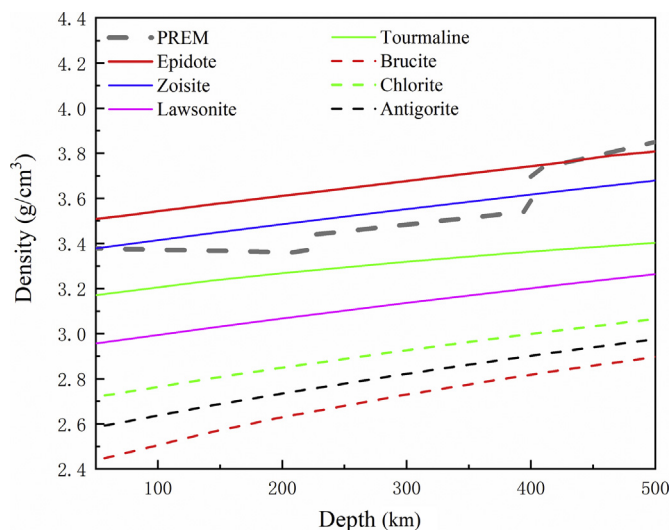


**Fig. 8.** Calculated density profiles of epidote and other hydrous minerals to ~500 km along the Tonga slab geotherm, and the PREM model (Dziewonski and Anderson, 1981) (color online).

the transition interval would be approximately 22 km wide if upper mantle olivine contained 500 ppm water. Moreover, Tonga, one of the world's coldest subduction zones, exhibits a more marked increase in seismic moment release near a depth of 400 km than other subduction zones (Bina and Navrotsky, 2000). As generally claimed (Green and Houston, 1995; Kirby et al., 1996), seismicity at and above such depths is related to water. This water is likely to be related to the dehydration reaction of hydrous minerals, such as epidote, near the 400 km depth beneath Tonga.

## 5. Conclusion

In summary, using *in situ* synchrotron-based single-crystal XRD at simultaneously high *P-T* conditions up to ~17.7 GPa and 700 K, we obtained the thermoelastic parameters of a natural epidote ( $X_{Ep} = 0.84$ ) and then modeled its density profile along a typical cold subduction geotherm. Comparing the density of epidote with those of other hydrous minerals, we found that epidote is the densest of these hydrous minerals and is more conducive to transporting water to deeper locations in the Earth's interior. Furthermore, during subduction, epidote may maintain the metastable state to ~14 GPa under the conditions of the coldest subduction zones, Tonga. Therefore, the water released from epidote under this pressure condition may potentially affect the properties of the 410 km seismic discontinuity. Moreover, as the density of PREM is larger than that of epidote group minerals at 410 km, epidote group minerals could favor slab stagnation above the 410 km discontinuity.

## Declaration of competing interest

The authors declare that they have no known competing financial interests or personal relationships that could have appeared to influence the work reported in this paper.

## Acknowledgments

Data of this paper is available at <https://zenodo.org/record/3387296#.XXERluzaw4>. We would like to thank two anonymous reviewers for their thorough and helpful comments. We thank Sergey N. Tkachev for the neon gas-loading assistance. This project was supported by the National Natural Science Foundation of China (Grant Nos. 41772043 and 41802043), the CAS "Light of West China" Program (2017 and 2019), the Youth Innovation Promotion

Association CAS (Dawei Fan, 2018434), and the Innovation and Entrepreneurship Funding of High-Level Overseas Talents of Guizhou Province (Dawei Fan, [2019]10). This work was performed at GeoSoilEnviroCARS (The University of Chicago, Sector 13), Advanced Photon Source (APS), Argonne National Laboratory. GeoSoilEnviroCARS is supported by the National Science Foundation (EAR-0622171) and the Department of Energy (DE-FG02-94ER14466) under Contract No. DE-AC02-06CH11357. This research used resources at the Advanced Photon Source, a U.S. Department of Energy (DOE) Office of Science User Facility operated for the DOE Office of Science by Argonne National Laboratory under Contract No. DE-AC02-06CH11357.

## Appendix A. Supplementary data

Supplementary data to this article can be found online at <https://doi.org/10.1016/j.gsf.2020.05.022>.

## References

- Agrusta, R., Hunen, J.V., Goes, S., 2015. The effect of metastable pyroxene on the slab dynamics. *Geophys. Res. Lett.* 41, 8800–8808.
- Alvaro, M., Angel, R.J., Camara, F., 2012. High-pressure behavior of zoisite. *Am. Mineral.* 97, 1165–1176.
- Allen, L.C., 1989. Electronegativity is the average one-electron energy of the valence-shell electrons in ground-state free atoms. *J. Am. Chem. Soc.* 111 (25), 9003–9014.
- Angel, R.J., 2000. Equation of State. In: Hazen, R.M., Downs, R.T. (Eds.), *High-Temperature and High-Pressure Crystal Chemistry, Reviews in Mineralogy and Geochemistry*, Mineralogical Society of America and Geochemical Society (Washington, DC), 41, pp. 35–59.
- Angel, R.J., Alvaro, M., Gonzalez-Platas, J., 2014. EosFit7c and a Fortran module (library) for equation of state calculations. *Z. für Kristallogr. - Cryst. Mater.* 229, 405–419.
- Angel, R.J., Bujak, M., Zhao, J., Gatta, G.D., Jacobsen, S.D., 2007. Effective hydrostatic limits of pressure media for high-pressure crystallographic studies. *J. Appl. Crystallogr.* 40, 26–32.
- Bina, C.R., 2016. Mineralogy: garnet goes hungry. *Nat. Geosci.* 6, 335–336.
- Bina, C.R., Navrotsky, A., 2000. Possible presence of high-pressure ice in cold subducting slabs. *Nature* 408, 844–847.
- Bindi, L., Bendeliani, A., Bobrov, A., Matrosova, E., Irifune, T., 2020. Incorporation of Mg in phase Egg,  $AlSi_3O_8OH$ : toward a new polymorph of phase H,  $MgSi_2O_4$ , a carrier of water in the deep mantle. *Am. Mineral.* 105 (1), 132–135.
- Bird, D.K., Spieler, A.R., 2004. Epidote in geothermal systems. *Rev. Mineral. Geochem.* 56, 235–300.
- Cao, Y., Song, S.G., 2009. Deformation and metamorphism of HP belt in the North Qilian Mountains and their implications for exhumation. *Acta Petrol. Sin.* 25, 2235–2246 (in Chinese with English abstract).
- Chen, A.P., Yang, J.J., Zhong, D.L., Shi, Y.H., Liu, J.B., 2019. Epidote spherulites and radial euhedral epidote aggregates in a greenschist facies metavolcanic breccia hosting an UHP eclogite in Dabieshan (China): implication for dynamic metamorphism. *Am. Mineral.* 104 (8), 1197–1212.
- Comodi, P., Zanazzi, P.F., 1997. The pressure behavior of clinozoisite and zoisite: an X-ray diffraction study. *Am. Mineral.* 82, 61–68.
- Dera, P., Zhuravlev, K., Prakapenka, V., Rivers, M.L., Finkelstein, G.J., Grubor-Urošević, O., Tschauer, O., 2013. High pressure single-crystal micro X-ray diffraction analysis with GSE\_ADA/RSV software. *High Pres. Res.* 33, 466–484.
- Dziewonski, A.M., Anderson, D.L., 1981. Preliminary reference Earth model. *Phys. Earth Planet. In.* 25, 297–356.
- Enami, M., Liou, J., Mattinson, C., 2004. Epidote minerals in high *P/T* metamorphic terranes: subduction zone and high- to ultrahigh-pressure metamorphism. *Rev. Mineral. Geochem.* 56, 347–398.
- Ewart, A., Collerson, K., Regelous, M., Wendt, J., Niu, Y., 1998. Geochemical evolution within the Tonga–Kermadec–Lau arc–back-arc systems: the role of varying mantle wedge composition in space and time. *J. Petrol.* 39, 331–368.
- Faccenda, M., 2014. Water in the slab: a trilogy. *Tectonophysics* 614, 1–30.
- Fan, D.W., Zhou, W.G., Wei, S.Y., Liu, Y.G., Ma, M.N., Xie, H.S., 2010. A simple external resistance heating diamond anvil cell and its application for synchrotron radiation X-ray diffraction. *Rev. Sci. Instrum.* 81, 053903.
- Fan, D.W., Ma, M.N., Yang, J.J., Wei, S.Y., Chen, Z.Q., Xie, H.S., 2011. In situ high-pressure synchrotron X-ray diffraction study of clinozoisite. *Chin. Phys. Lett.* 28 (12), 126103.
- Fan, D.W., Ma, M.N., Wei, S.Y., Chen, Z.Q., Xie, H.S., 2013a. In-situ synchrotron powder X-ray diffraction study of vanadinite at room temperature and high pressure. *High. Temp. - High. Press.* 42, 441–449.
- Fan, D.W., Wei, S.Y., Liu, J., Li, Y.C., Xie, H.S., 2013b. X-ray diffraction study of calcium-lead fluorapatite solid solution at high pressure: the composition dependence of the bulk modulus and its pressure derivative. *High. Temp. - High. Press.* 42, 69–80.
- Fan, D.W., Xu, J.G., Wei, S.Y., Chen, Z.Q., Xie, H.S., 2014. In-situ high-pressure synchrotron X-ray diffraction of natural epidote. *Chin. J. High Press. Phys.* 28, 257–261 (in Chinese with English abstract).
- Fan, D., Xu, J., Ma, M., Wei, S., Zhang, B., Liu, J., Xie, H., 2015. *P-V-T* equation of state of  $Ca_3Cr_2Si_3O_{12}$  uvarovite garnet by using a diamond-anvil cell and in-situ synchrotron X-ray diffraction. *Am. Mineral.* 100, 588–597.



- Fan, D.W., Fu, S.Y., Yang, J., Tkachev, S.N., Prapakpenka, V.B., Lin, J.F., 2019a. Elasticity of single-crystal periclase at high pressure and temperature: the effect of iron on the elasticity and seismic parameters of ferropericlase in the lower mantle. *Am. Mineral.* 104, 262–275.
- Fan, D.W., Xu, J.G., Lu, C., Tkachev, S.N., Li, B., Ye, Z.L., Huang, S.J., Prapakpenka, V.B., Zhou, W.G., 2019b. Elasticity of single-crystal low water content hydrous pyrope at high-pressure and high-temperature conditions. *Am. Mineral.* 104, 1022–1031.
- Fehr, K.T., Heuss-Aßbichler, S., 1997. Intracrystalline equilibria and im-miscibility along the join clinozoisite-epidote: an experimental and  $^{57}\text{Fe}$  Mössbauer study. *Neues Jahrbuch Mineral. Abhand.* 172, 43–67.
- Fei, Y., 1995. Thermal Expansion, Mineral Physics & Crystallography: a Handbook of Physical Constants. American Geophysical Union, pp. 29–44.
- Fei, Y.W., Ricolleau, A., Frank, M., Mibe, K., Shen, G.Y., Prapakpenka, V., 2007. Toward an internally consistent pressure scale. In: *Proceedings of the National Academy of Sciences of the United States of America*, vol. 104, pp. 9182–9186.
- Ferrando, S., Frezzotti, M.L., Dallai, L., Compagnoni, R., 2005. Fluid-rock interaction in UHP phengite-kyanite-epidote eclogite from the Sulu orogen, eastern China. *Int. Geol. Rev.* 47, 750–774.
- Formeris, J.F., Holloway, J.R., 2003. Phase equilibria in subducting basaltic crust: implications for  $\text{H}_2\text{O}$  release from the slab. *Earth Planet Sci. Lett.* 214, 187–201.
- Franz, G., Liebscher, A., 2004. Physical and chemical properties of the epidote minerals—an introduction. *Rev. Mineral. Geochem.* 56, 1–81.
- Frei, D., Liebscher, A., Franz, G., Dulski, P., 2004. Trace element geochemistry of epidote minerals. *Rev. Mineral. Geochem.* 56, 553–605.
- Ganguly, J., Freed, A.M., Saxena, S.K., 2009. Density profiles of oceanic slabs and surrounding mantle: integrated thermodynamic and thermal modeling, and implications for the fate of slabs at the 660 km discontinuity. *Phys. Earth Planet. In.* 172, 257–267.
- Gatta, G.D., Merlini, M., Lee, Y., Poli, S., 2011. Behavior of epidote at high pressure and high temperature: a powder diffraction study up to 10 GPa and 1,200 K. *Phys. Chem. Miner.* 38, 419–428.
- Gottschalk, M., 2004. Thermodynamic properties of zoisite, clinozoisite and epidote. *Rev. Mineral. Geochem.* 56, 83–124.
- Green, H.W., Houston, H., 1995. The mechanics of deep earthquakes. *Annu. Rev. Earth Planet Sci.* 23, 169–213.
- Grevel, K.D., Nowlan, E.U., Fasshauer, D.W., Burchard, M., 2000. In situ X-ray diffraction investigation of lawsonite and zoisite at high pressures and temperatures. *Am. Mineral.* 85, 206–216.
- Guo, S., Ye, K., Wu, T., Chen, Y., Yang, Y., Zhang, L., Liu, J., Mao, Q., Ma, Y., 2013. A potential method to confirm the previous existence of lawsonite in eclogite: the mass imbalance of Sr and LREEs in multistage epidote (Ganghe, Dabie UHP terrane). *J. Metamorph. Geol.* 31, 415–435.
- Hacker, B.R., Peacock, S.M., Abers, G.A., Holloway, S.D., 2003. Subduction factory 2. Are intermediate-depth earthquakes in subducting slabs linked to metamorphic dehydration reactions? *J. Geophys. Res.* 108, 20–30.
- Holland, T., Redfern, S., 1997. Unit cell refinement from powder diffraction data: the use of regression diagnostics. *Mineral. Mag.* 61, 65–77.
- Holland, T.J.B., Redfern, S.A.T., Pawley, A.R., 1996. Volume behavior of hydrous minerals at high pressure and temperature; II, Compressibilities of lawsonite, zoisite, clinozoisite, and epidote. *Am. Mineral.* 81, 341–348.
- Huang, S., Chen, J., 2014. Equation of state of pyrope-almandine solid solution measured using a diamond anvil cell and in situ synchrotron X-ray diffraction. *Phys. Earth Planet. In.* 228, 88–91.
- Kakizawa, S., Inoue, T., Nakano, H., Kuroda, M., Sakamoto, N., Yurimoto, H., 2018. Stability of Al-bearing superhydrous phase B at the mantle transition zone and the uppermost lower mantle. *Am. Mineral.* 103 (8), 1221–1227.
- Kantor, I., Prapakpenka, V., Kantor, A., Dera, P., Kurnosov, A., Sinogeikin, S., Dubrovinskaya, N., Dubrovinsky, L., 2012. BX90: a new diamond anvil cell design for X-ray diffraction and optical measurements. *Rev. Sci. Instrum.* 83, 125102. <https://doi.org/10.1063/1.4768541>.
- King, S.D., Frost, D.J., Rubie, D.C., 2015. Why cold slabs stagnate in the transition zone. *Geology* 43, 231–234.
- Kirby, S.H., Stein, S., Okal, E.A., Rubie, D.C., 1996. Metastable mantle phase transformations and deep earthquakes in subducting oceanic lithosphere. *Rev. Geophys.* 34, 261–306.
- Liou, J., 1973. Synthesis and stability relations of epidote,  $\text{Ca}_2\text{Al}_2\text{FeSi}_3\text{O}_{12}(\text{OH})$ . *J. Petrol.* 14, 381–413.
- Liou, J., 1993. Stabilities of natural epidotes. *Abh. Geol. Bundesanst.* 49, 7–16.
- Liu, D., Pang, Y.W., Ye, Y., Jin, Z.M., Smyth, J.R., Yang, Y., Zhang, Z.M., Wang, Z.P., 2019a. In-situ high-temperature vibrational spectra for synthetic and natural clinohumite: implications for dense hydrous magnesium silicates in subduction zones. *Am. Mineral.* 104 (1), 53–63.
- Liu, T., Wang, D.J., Shen, K.W., Liu, C.J., Yi, L., 2019b. Kinetics of antigorite dehydration: rapid dehydration as a trigger for lower-plane seismicity in subduction zones. *Am. Mineral.* 104 (2), 282–290.
- Liu, X.C., Matsukage, K.N., Nishihara, Y., Suzuki, T., Takahashi, E., 2019c. Stability of the hydrous phases of Al-rich phase D and Al-rich phase H in deep subducted oceanic crust. *Am. Mineral.* 104 (1), 64–72.
- Mao, Z., Fan, D.W., Lin, J.F., Yang, J., Tkachev, S.N., Zhuravlev, K., Prapakpenka, V.B., 2015. Elasticity of single-crystal olivine at high pressures and temperatures. *Earth Planet Sci. Lett.* 426, 204–215.
- Mierlo, W.L.V., Langenhorst, F., Frost, D.J., Rubie, D.C., 2013. Stagnation of subducting slabs in the transition zone due to slow diffusion in majoritic garnet. *Nat. Geosci.* 6, 400–403.
- Mookherjee, M., Panero, W.R., Wunder, B., Jahn, S., 2019. Anomalous elastic behavior of phase egg,  $\text{AlSiO}_3(\text{OH})$ , at high pressures. *Am. Mineral.* 104 (1), 130–139.
- O'Bannon III, E., Beavers, C.M., Kunz, M., Williams, Q., 2018. High-pressure study of dravite tourmaline: insights into the accommodating nature of the tourmaline structure. *Am. Mineral.* 103, 1622–1633.
- Pawley, A.R., Chinnery, N.J., Clark, S.M., 1998. Volume measurements of zoisite at simultaneously elevated pressure and temperature. *Am. Mineral.* 83, 1030–1036.
- Pawley, A.R., Clark, S.M., Chinnery, N.J., 2002. Equation of state measurements of chlorite pyrophyllite and talc. *Am. Mineral.* 87, 1172–1182.
- Pawley, A.R., Redfern, S.A.T., Holland, T.J.B., 1996. Volume behavior of hydrous minerals at high pressure and temperature; I, Thermal expansion of lawsonite, zoisite, clinozoisite, and diaspore. *Am. Mineral.* 81, 335–340.
- Peacock, S.A., 1990. Fluid processes in subduction zones. *Science* 248, 329–337.
- Peacock, S.M., 2001. Are the lower planes of double seismic zones caused by serpentine dehydration in subducting oceanic mantle? *Geology* 29, 299–302.
- Peacock, S.M., Hyndman, R.D., 1999. Hydrous minerals in the mantle wedge and the maximum depth of subduction thrust earthquakes. *Geophys. Res. Lett.* 26, 2517–2520.
- Poli, S., Schmidt, M.W., 2004. Experimental subsolidus studies on epidote minerals. *Rev. Mineral. Geochem.* 56, 171–195.
- Portnyagin, M., Hoernle, K., Plechov, P., Mironov, N., Khubunaya, S., 2007. Constraints on mantle melting and composition and nature of slab components in volcanic arcs from volatiles ( $\text{H}_2\text{O}$ , S, Cl, F) and trace elements in melt inclusions from the Kamchatka Arc. *Earth Planet Sci. Lett.* 255, 53–69.
- Qin, F., Wu, X., Wang, Y., Fan, D., Qin, S., Yang, K., Townsend, J.P., Jacobsen, S.D., 2016. High-pressure behavior of natural single-crystal epidote and clinozoisite up to 40 GPa. *Phys. Chem. Miner.* 43, 649–659.
- Qin, S., Wu, X., Liu, J., Liu, J., Wu, Z.Y., Li, X.D., Lu, A.H., 2003. Compressibility of epidote up to 20 GPa at 298 K. *Chin. Phys. Lett.* 20, 1172–1174.
- Rivers, M., Prapakpenka, V.B., Kubo, A., Pullins, C., Holl, C.M., Jacobsen, S.D., 2008. The COMPRES/GSECARS gas-loading system for diamond anvil cells at the Advanced Photon Source. *High Pres. Res.* 28, 273–292.
- Satta, N., Marquardt, H., Kurnosov, A., Buchen, J., Kawazoe, T., McCammon, C., Ballaran, T.B., 2019. Single-crystal elasticity of iron-bearing phase E and seismic detection of water in Earth's upper mantle. *Am. Mineral.* 104 (10), 1526–1529.
- Schmidt, M.W., Poli, S., 1998. Experimentally based water budgets for dehydrating slabs and consequences for arc magma generation. *Earth Planet Sci. Lett.* 163, 361–379.
- Sinogeikin, S., Bass, J., Prapakpenka, V., Lakshtanov, D., Shen, G.Y., Sanchez-Valle, C., Rivers, M., 2006. Brillouin spectrometer interfaced with synchrotron radiation for simultaneous X-ray density and acoustic velocity measurements. *Rev. Sci. Instrum.* 77, 103905.
- Spandler, C., Hermann, J., Arculus, R., Mavrogenes, J., 2003. Redistribution of trace elements during prograde metamorphism from lawsonite blueschist to eclogite facies; implications for deep subduction-zone processes. *Contrib. Mineral. Petrol.* 146, 205–222.
- Vinet, P., Ferrante, J., Smith, J., Rose, J., 1986. A universal equation of state for solids. *J. Phys. Condens. Matter* 19, L467.
- Wood, B.J., Pawley, A., Frost, D.R., 1996. Water and carbon in the Earth's mantle. *Philosoph. Trans. Royal Soc. Lond. Phil. Trans. R. Soc. A* 354, 1495–1511.
- Xia, X., Weidner, D.J., Zhao, H., 1998. Equation of state of brucite: single-crystal Brillouin spectroscopy study and polycrystalline pressure-volume-temperature measurement. *Am. Mineral.* 83, 68–74.
- Xu, J., Kuang, Y., Zhang, B., Liu, Y., Fan, D., Li, X., Xie, H., 2016. Thermal equation of state of natural tourmaline at high pressure and temperature. *Phys. Chem. Miner.* 43, 315–326.
- Xu, C.W., Nishi, M., Inoue, T., 2019a. Solubility behavior of  $\delta\text{-AlOOH}$  and  $\epsilon\text{-FeOOH}$  at high pressures. *Am. Mineral.* 104, 1416–1420.
- Xu, J.G., Zhang, D.Z., Dera, P., Zhang, B., Fan, D.W., 2017a. Experimental evidence for the survival of augite to transition zone depths, and implications for subduction zone dynamics. *Am. Mineral.* 102, 1516–1524.
- Xu, J.G., Zhang, D.Z., Fan, D.W., Downs, R.T., Hu, Y., Dera, P.K., 2017b. Isosymmetric pressure-induced bonding increase changes compression behavior of clinopyroxenes along jadeite-aegirine solid solution in subduction zones. *J. Geophys. Res.: Solid Earth* 122, 142–157.
- Xu, J.G., Zhang, D.Z., Fan, D.W., Zhang, J.S., Zhou, W.G., 2018. Phase transitions in orthoenstatite and subduction zone dynamics: effects of water and transition metal ions. *J. Geophys. Res.: Solid Earth* 123, 2723–2737.
- Xu, J.G., Zhang, D.Z., Fan, D.W., Dera, P., Shi, F., Zhou, W.G., 2019b. Thermoelastic properties of eclogitic ternary garnets and omphacites: implications for deep subduction of oceanic crust and density anomalies in the upper mantle. *Geophys. Res. Lett.* 46, 179–188.
- Yang, C.P., Inoue, T., Yamada, A., Kikegawa, T., Ando, J.-i., 2014a. Equation of state and phase transition of antigorite under high pressure and high temperature. *Phys. Earth Planet. In.* 228, 56–62.
- Yang, J., Mao, Z., Lin, J.F., Prapakpenka, V.B., 2014b. Single-crystal elasticity of the deep-mantle magnesite at high pressure and temperature. *Earth Planet Sci. Lett.* 392, 292–299.
- Zhang, D.Z., Dera, P.K., Eng, P.J., Stubbs, J.E., Zhang, J.S., Prapakpenka, V.B., Rivers, M.L., 2017. High pressure single crystal diffraction at PX<sup>2</sup>. *J. Vis. Exp.* 119, e54660. <https://doi.org/10.3791/54660>.
- Zhang, L., Smyth, J.R., Kawazoe, T., Jacobsen, S.D., Niu, J.J., He, X.J., Qin, S., 2019. Stability, composition, and crystal structure of Fe-bearing Phase E in the transition zone. *Am. Mineral.* 104 (11), 1620–1624.
- Zhang, J.Z., 1999. Room-temperature compressibilities of MnO and CdO: further examination of the role of cation type in bulk modulus systematics. *Phys. Chem. Miner.* 26, 644–648.
- Zheng, Y.F., Chen, R.X., Xu, Z., Zhang, S.B., 2016. The transport of water in subduction zones. *Sci. China Earth Sci.* 59, 651–682.
- Zheng, Y.F., 2019. Subduction zone geochemistry. *Geosci. Front.* 10, 1223–1254.